



Hot Surface Ignition of *n*-Hexane Mixtures Using Simplified Kinetics

Josué Melguizo-Gavilanes, Augustin Nové-Josserand, Stephanie Coronel, Rémy Mével, and Joseph E. Shepherd

Graduate Aerospace Laboratories, California Institute of Technology (GALCIT), Pasadena, California, USA

ABSTRACT

Hot surface ignition is relevant in the context of industrial safety. In the present work, two-dimensional simulations using simplified kinetics of the buoyancy-driven flow and ignition of a slightly lean *n*-hexane–air mixture by a rapidly heated surface (glowplug) are reported. Experimentally, ignition is most often observed to occur at the top of the glowplug; numerical results reproduce this trend and shed light on this behavior. The numerical predictions of the flow field and hot surface temperature at ignition are in quantitative agreement with experiments. The simulations suggest that flow separation plays a crucial role in creating zones where convective losses are minimized and heat diffusion is maximized, resulting in the critical conditions for ignition to take place.

ARTICLE HISTORY

Received 4 November 2015

Revised 7 April 2016

Accepted 1 May 2016

KEYWORDS

n-Hexane; Hot surface ignition; Industrial safety; Simplified kinetics

Introduction

Accidental ignition of combustible atmospheres by hot surfaces is a major concern in industrial safety. Determining critical conditions for ignition in terms of surface size and temperature are essential to evaluating the potential of an ignition hazard. Classical experimental work on hot surface ignition includes that of Coward and Guest (1927) and Kuchta (1985). The former investigated the effect of material (e.g., catalytic and noncatalytic surfaces) on ignition thresholds, whereas the latter extended this work to study the effect of size and geometry. The impact of their results was hindered by their inability to measure flow velocity and composition during the ignition event. Additionally, experimental work done by Boettcher (2012) using a glowplug, found the ignition temperature for *n*-hexane to be essentially insensitive to composition away from the flammability limits. In analytical studies, the typical approach is to reduce the ignition problem to a steady one-dimensional (1D) energy equation with a source term accounting for the heat release from chemical reactions. Seminal work on thermal ignition theory was done by Semenov (1940) who derived an analytical expression for ignition temperature as a function of surface area. Kuchta et al. (1965) extended and simplified Semenov's findings. Gray (1970) investigated the effect of surface to volume ratio on ignition of negative temperature coefficient (NTC) fuels; Law and Law (1979) solved the steady boundary layer equations for mixtures with high activation energy using matched asymptotics; and, more recently, Laurendeau (1982) proposed a simple model to estimate the minimum ignition temperature. Some numerical efforts in this area are due to Kumar (1989),

CONTACT Josué Melguizo-Gavilanes ✉ josuemg@caltech.edu Graduate Aerospace Laboratories, California Institute of Technology (GALCIT), 1200 E. California Blvd., Pasadena, CA 91125, USA.

Color versions of one or more of the figures in the article can be found online at <http://www.tandfonline.com/gcst>

© 2016 Taylor & Francis

who developed a 1D model to study hydrogen ignition, and Adler (1999), who performed 2D steady simulations of a circular hot spot in contact with a reactive mixture. Also, Boettcher (2012) focused on capturing lower flammability limits with tabulated chemistry, and studying the effect of hot surface area on ignition temperature. The previous work has not been concerned with analyzing in detail the flow field in the vicinity of the hot surface.

Simulation of hot surface ignition is challenging due to the wide range of temporal and spatial scales involved, and the size of detailed chemical kinetic mechanisms — large hydrocarbon fuels conventionally used in industry typically comprise thousands of reactions and hundreds of species. For an accurate prediction, it is necessary to solve the conservation equations together with transport of chemical species on a mesh small enough to capture the thermal and hydrodynamic boundary layers surrounding the hot surface. To make the problem computationally tractable, a detailed numerical simulation of the transient viscous flow and ignition of combustible atmospheres by a rapidly heated surface using simplified chemistry is presented. Particularly, one of the observations made by Boettcher (2012) and confirmed recently during an additional experimental campaign carried out at Caltech with the same setup but using improved surface temperature measurement diagnostics requires further study. In the experiments reported by Boettcher (2012) using *n*-hexane–air mixtures, 53% of ignition events were observed to occur at the top of the glowplug, 30% were reported to have taken place on the side of the hot surface, and 17% in the thermal plume that develops as a consequence of the buoyancy-driven flow induced. In our experiments, however, for all conditions tested, ignition always occurred at the top of the hot surface; why is ignition more likely to occur at the top? This study aims to answer this question and to understand the physics driving this behavior. Special attention is given to the near-wall buoyancy flow induced, and flow separation to gain insight on the dynamics, time, and location of the ignition event.

Physical model, numerical approach, and simulation parameters

The heat transfer and ignition process in the gas is governed by the variable-density reactive Navier–Stokes equations with temperature-dependent transport properties:

$$\frac{\partial \rho}{\partial t} + \nabla \cdot (\rho \mathbf{u}) = 0 \quad (1)$$

$$\frac{\partial (\rho \mathbf{u})}{\partial t} + \nabla \cdot (\rho \mathbf{u} \mathbf{u}) = -\nabla p + \nabla \cdot \boldsymbol{\tau} + \rho \mathbf{g} \quad (2)$$

$$\frac{\partial (\rho h_s)}{\partial t} + \nabla \cdot (\rho \mathbf{u} h_s) = \nabla \cdot (\kappa / c_p \nabla h_s) + q_{chem} \dot{\Omega}_R \quad (3)$$

$$\text{with } p = \rho \bar{R}T, \quad \boldsymbol{\tau} = \mu \left[\nabla \mathbf{u} + (\nabla \mathbf{u})^T \right] - \frac{2}{3} \mu (\nabla \cdot \mathbf{u}) \mathbf{I} \quad (4)$$

The Sutherland Law, the Eucken Relation, and the JANAF polynomials are used to account for the functional temperature dependence of mixture viscosity (μ), thermal conductivity (κ), and specific heat (c_p), respectively. The chemistry is modeled using an irreversible one-step scheme ($R \rightarrow P$) in which the kinetic parameters are fitted to match the ignition delay times of the updated Ramirez's detailed mechanism (Ramirez et al.,

2011) referred to as Mével's model (Mével et al., 2014) at $p_o = 101$ kPa and equivalence ratio $\Phi = 0.9$ for $900\text{ K} < T < 1600\text{ K}$. Figure 1 shows the comparison of the ignition delay times obtained with the detailed mechanism and those obtained with the one-step model.

Using subscript R for reactants, species mass conservation can then be written as:

$$\frac{\partial(\rho Y_R)}{\partial t} + \nabla \cdot (\rho \mathbf{u} Y_R) = \nabla \cdot (\rho D_R \nabla Y_R) + \dot{\Omega}_R \text{ with } \dot{\Omega}_R = -\rho Y_R A T^b \exp(-E/R_u T) \quad (5)$$

In Eqs. (1)–(5), ρ is density, \mathbf{u} is the velocity vector, p is pressure, h_s is the mixture sensible enthalpy, g is the gravitational acceleration, q_{chem} is the stored chemical energy, $\dot{\Omega}_R$ is the rate of consumption of reactants, \mathbf{I} is the identity matrix, Y_R is the mass fraction of reactants, A is the pre-exponential factor, b is the temperature exponent in the modified Arrhenius rate law, E is the activation energy, and R_u and \bar{R} are the universal and specific gas constants, respectively. The Lewis number is assumed to be unity, which results in $\kappa/c_p = \rho D_R$; hence, the dynamic thermal diffusivity of reactants is used to model its mass diffusivity.

The equations above are integrated in two dimensions using the open source field operation and manipulation (OpenFOAM) toolbox (Weller et al., 1998). The spatial discretization of the solution domain is done using finite volumes, and the pressure-velocity coupling is achieved using the PIMPLE (PISO+SIMPLE) algorithm (Demirdzic et al., 1993). The geometry simulated corresponds to that used by Boettcher (2012), a combustion vessel of $11.4\text{ cm} \times 17.1\text{ cm}$ with a glowplug of $9.3\text{ mm} \times 5.1\text{ mm}$ located in the center. Figure 2 shows a schematic of the vessel together with a close-up of the glowplug geometry. There are approximately 200,000 cells in the 2D-axisymmetric computational domain, compressed

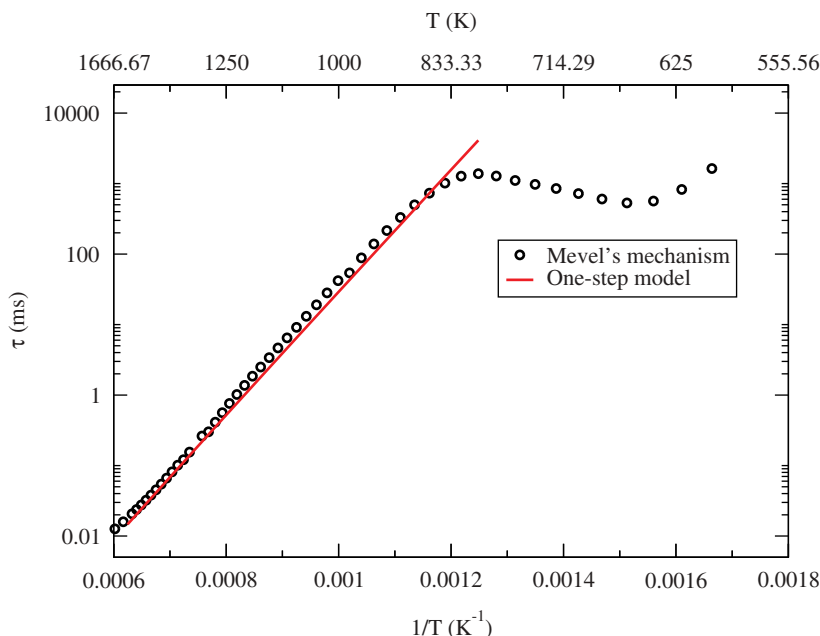


Figure 1. Comparison of ignition delay times obtained with Mével's mechanism (circles) and those obtained using the one-step model (solid red line).

near the wall of the glowplug, with a minimum cell size of $80\mu\text{m}$ to resolve the thermal and hydrodynamic boundary layers. The initial conditions are $p_o = 101\text{ kPa}$, $T_o = 300\text{ K}$, $\mathbf{u}_o = (0, 0, 0)\text{ m/s}$, and $Y_{Ro} = 1$, with no-slip and adiabatic boundary condition on the vessel walls, and a prescribed temperature ramp on the surface of the glowplug given by $T(t) = T_o + rt$ with $r = 220\text{ K/s}$ as was experimentally measured in Boettcher (2012). The chemical kinetics parameters used for modeling a slightly lean ($\Phi = 0.9$) *n*-hexane-air mixture are $q_{chem} = 2.461 \times 10^6\text{ J/kg}$, $E = 158,282\text{ J/mol}$, $A = 0.1618\text{ s}^{-1}\text{ K}^{-2.989}$, and $b = 2.989$.

Results

Experimental results

The experiments performed by Boettcher (2012) were repeated using a smaller field of view, focusing only on the upper region of the glowplug, and with improved diagnostics to capture the ignition event. The inside of the combustion vessel (see Figure 2) is a rectangular prism with inner dimensions of $11.4\text{ cm} \times 11.4\text{ cm} \times 17.1\text{ cm}$ (width \times depth \times height) giving an internal volume of approximately two liters. Four access ports, including two windows of 59.9 mm in diameter, allow for interferometry (Mach–Zehnder interferometer for visualization of the flow field) and simultaneous access for temperature measurements using pyrometry (two-color pyrometer for hot surface temperature measurements). The interferograms obtained represent the optical path length difference between light traveling through a field of view with refractivity $n(z)$ and light traveling through a reference field with refractivity $n_0(z)$. The coordinate system relative to the combustion vessel is shown in Figure 2 (left).

The difference in phase, $\Delta\phi$, is related to the index of refraction by:

$$\Delta\phi = \phi - \phi_0 = \frac{2\pi}{\lambda} \int_{\zeta_1}^{\zeta_2} [n(z) - n_0(z)] dz \quad (6)$$

where ζ_1 and ζ_2 are the locations along the z -axis where a ray of light enters and leaves the test section, respectively, and λ is the wavelength of the light in a vacuum. In the current study, $\lambda = 5.32 \times 10^{-7}\text{ m}$. The intensity, I , of a 2D fringe pattern is represented by an amplitude and frequency modulated function:

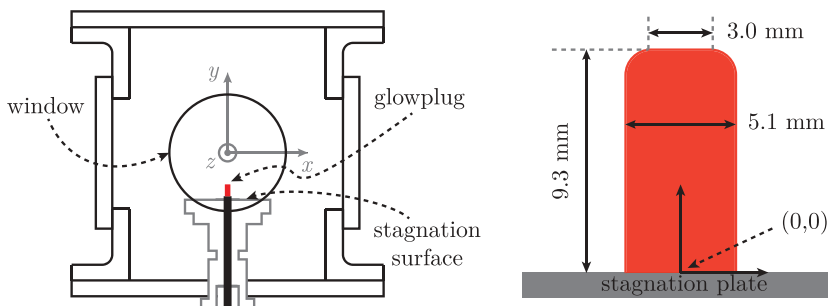


Figure 2. Left: diagram of combustion vessel, glowplug mounting fixture with stagnation surface, field of view (FOV), and glowplug (in red); dimensions in mm. Right: Autolite glowplug schematic.

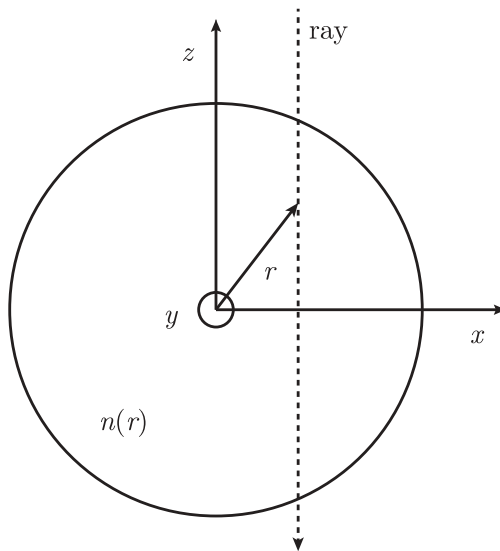


Figure 3. Schematic of generic field of view showing coordinate system, cylindrical symmetry assumption, and Abel transform variables.

$$I(x, y) = a(x, y) + b(x, y) \cos(\Delta\varphi(x, y)) \quad (7)$$

where a represents the background illumination and noise, b is the amplitude, and φ is the phase (Rastogi and Hack, 2015). The phase demodulation of the interferograms, i.e., obtaining $\Delta\varphi$, is accomplished by using the 2D windowed Fourier filtering method (WFF2; Kemao, 2004).

Further analysis can be performed on the optical phase difference ($\Delta\varphi$) to obtain a more familiar quantity, such as density (ρ). If the index of refraction is assumed to be cylindrically symmetric, as indicated in Figure 3, the inverse Abel transform (Nestor and Olsen, 1960), Eq. (8), can be used to relate a line of sight integrated quantity, $\Delta\varphi$, to a radially distributed one, $n(r)$. The refractive index, $n(r)$, can then be related to the density through the use of the Gladstone–Dale relation shown in Eq. (9):

$$f(r) = \frac{2\pi}{\lambda} [n(r) - n_o(r)] = -\frac{1}{\pi} \int_r^\infty \frac{dF(x)}{dx} \frac{dx}{(x^2 - r^2)^{1/2}} \quad \text{where } F(x) = \Delta\varphi \quad (8)$$

$$n - 1 = K\rho \quad (9)$$

In the present study, no attempts are made to use Eq. (8) to extract $n(r)$ due to the high sensitivity of the equation to fluctuations in $\Delta\varphi$. It is worth mentioning that this post-processing technique is typically used in steady problems because the optical phase difference can be time averaged over multiple frames to obtain a smoother $\Delta\varphi$. In transient problems, like the one at hand, noise filtering is limited due to the lack of time averaging. Additionally, the inversion of the Abel transform accumulates errors as the integration is performed from the outermost layer, $n(r) = R$ (field of view radius), towards the center, $r = 0$, yielding higher errors at the axis of symmetry. For these reasons, we concluded the image processing after the optical phase difference was obtained instead

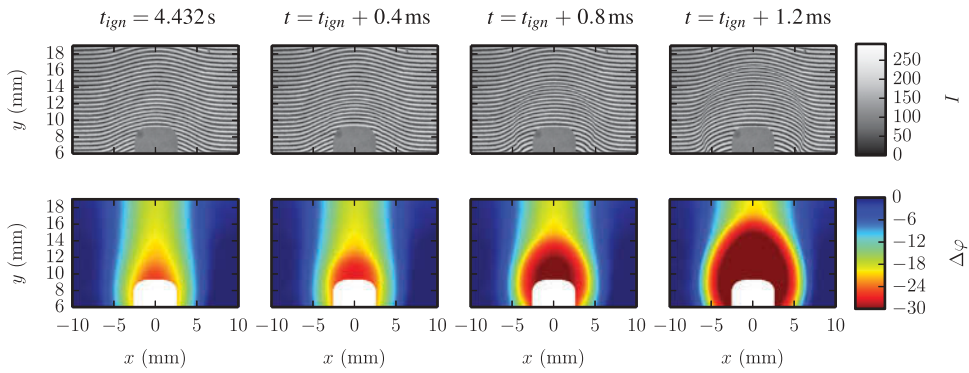


Figure 4. Ignition experiments at $p_o = 101$ kPa, $T_o = 300$ K, and $\Phi = 0.9$ *n*-hexane–air mixture. Surface temperature at ignition $T = 1275$ K \pm 45 K. Top: interferometry visualization (I). Bottom: optical phase difference ($\Delta\phi$).

of introducing large uncertainties in the results by performing the Abel transform inversion.

Experiments were carried out using *n*-hexane–air mixtures with equivalence ratios and initial pressures of $0.5 < \Phi < 3$, and $40 \text{ kPa} < p_o < 100 \text{ kPa}$, respectively. For each experiment the combustion vessel is evacuated and filled with *n*-hexane, oxygen, and nitrogen using the method of partial pressures to create the reactive mixture (0.01 kPa accurate). Uniform mixing of the mixture is achieved using a recirculation pump for 2 min, and then left to settle for an additional 2 min before imposing the temperature ramp on the hot surface. Figure 4 shows interferograms (top) and optical phase difference (bottom) of a typical ignition result. The conditions used for this shot are $p_o = 101$ kPa, $T_o = 300$ K, $r = 220$ K/s, and $\Phi = 0.9$. The top row shows a sequence of interferograms during ignition of the mixture. The fringe shift observed near the center corresponds to a density change in the flow field, the larger the shift, the larger the change in refractive index (or equivalently, the lower [higher] the density [temperature] is). In the first two images (from left to right), the thermal plume produced by the heating of the glowplug is seen as a smooth fringe shift. On the third and fourth images a greater shift occurs in the vicinity of the glowplug. The region of rapid change delineates the flame front that forms and propagates away from the top of the hot surface. The images on the bottom row show the optical phase difference ($\Delta\phi$) obtained from the interferograms. The ignition kernel is visible in the first two images as a dark red region above the glowplug. The flame shape is better defined in the subsequent images. A total of three experiments were performed at this condition, obtaining an average surface temperature at ignition of 1275 ± 45 K recorded by the pyrometer. Sources of uncertainty in the ignition surface temperature reported here include emissivity dependence on wavelength, and noise and calibration errors. The experimental results are summarized in Table 1.

Numerical results

Overview, flow structure, and temporal evolution

A detailed analysis of the flow field before ignition takes place has been performed to identify and quantify important features in the flow, such as thermal and hydrodynamic boundary layers, flow separation, thermal plume temperature, and velocity distributions.

Table 1. Experimental glowplug surface temperature at ignition for a slightly lean ($\Phi = 0.9$) *n*-hexane–air mixture at $p_o = 101$ kPa and $T_o = 300$ K.

Experiment	Glowplug surface temperature (K)	Lower bound (K)	Upper bound (K)
1	1271	1227	1317
2	1274	1230	1320
3	1280	1236	1326

Figure 5 (Left) shows the temperature and velocity (magnitude) fields obtained after 4s of heating, together with temperature isocontours taken every 100K from $400\text{ K} \leq T \leq 1180\text{ K}$, and velocity vectors showing clearly the buoyancy driven flow induced by the glowplug. Figure 5 (Right) shows plots of the spatial distribution of velocity (u_x , u_y , and u_{mag}) and temperature at two locations from the surface of the glowplug. The top plot displays the vertical spatial distribution starting at $(x = 0\text{ mm}, y = 9.3\text{ mm})$ immediately above the hot surface, whereas the bottom plot displays the horizontal spatial distribution starting at $(x = 2.55\text{ mm}, y = 5\text{ mm})$ on the side of the glowplug. The origin of the coordinate system ($x = 0\text{ mm}, y = 0\text{ mm}$) is located at the stagnation plate on the vertical centerline at the bottom of the glowplug (see Figure 2).

In the vicinity of the hot surface there is a thermal boundary layer and above the glowplug, a thermal plume. Note that in the separated region (above the glowplug) there is a thicker thermal layer. The thermal plume is delineated by the outermost temperature contour ($T = 400\text{ K}$). The velocity (magnitude) and velocity vectors illustrate the flow occurring near and above the glowplug. Parcels of fresh cold gas enter the thermal

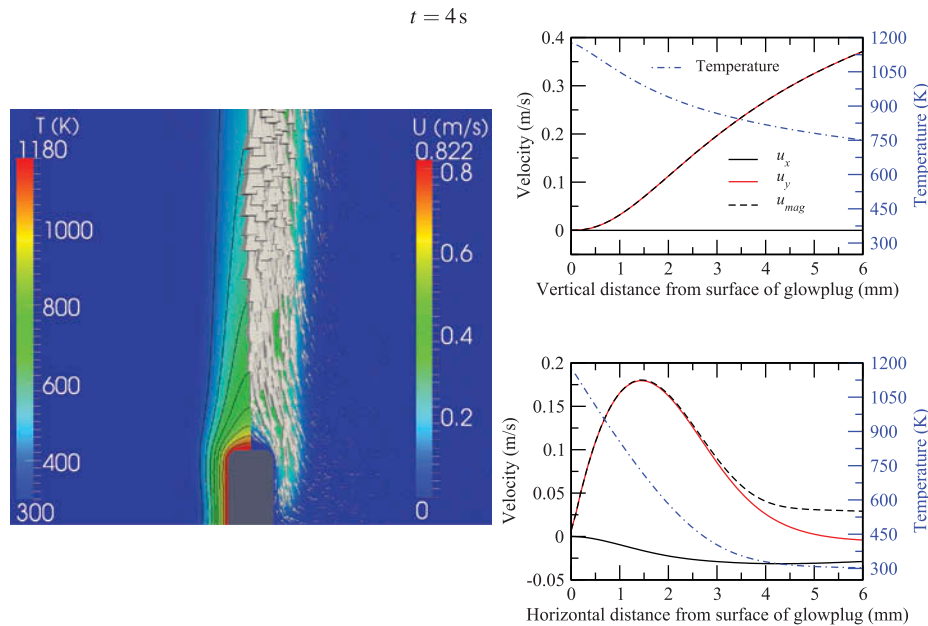


Figure 5. Left: temperature and velocity (magnitude) field in the vicinity of the glowplug, temperature isocontours, and velocity vectors. Right: spatial distribution of velocity and temperature at top—from $(x_o = 0\text{ mm}, y_o = 9.3\text{ mm})$ to $(x_f = 0\text{ mm}, y_f = 15.3\text{ mm})$, and side—from $(x_o = 2.55\text{ mm}, y_o = 5\text{ mm})$ to $(x_f = 8.55\text{ mm}, y_f = 5\text{ mm})$ of the glowplug.

boundary layer from below and heat up slowly as they travel upward in close proximity to the wall. Once the parcels of gas reach the upper right/left corner of the glowplug, the flow separates, creating a region at the top of the glowplug where the gas is practically at rest. The gas continues to rise to the top of the combustion vessel, which is forced to turn and creates a rather complex vortical flow field (not visible in Figure 5). Details of this flow field and an unusual cyclic flame oscillation were examined in experiments and simulations by Boettcher et al. (2013) for *n*-hexane–air mixtures in this geometry.

In Figure 5 (top right graph), the horizontal (u_x) and vertical (u_y) components of the velocity vector (black and red solid lines, respectively), magnitude (dashed line), and temperature (blue dashed-dotted line) confirm that up to 0.5 mm away from the top surface of the glowplug, the flow is essentially stagnant. As a result, the convective losses are minimal in this region. The plot also shows the temperature distribution of the thermal plume up to 6 mm away from the glowplug surface. At the side of the glowplug ($x = 2.55$ mm, $y = 5$ mm), Figure 5 (bottom right graph), the temperature and velocity magnitude plots show the thermal and hydrodynamic boundary layer thickness, 5.5 mm and 4 mm, respectively. The negative values of u_x (gas moving left) display how parcels of fluid are brought into the thermal boundary layer from colder regions away from the glowplug, slowed as they approach the hot surface, changing direction gradually (see increase in u_y), subsequently reaching a maximum, immediately followed by a decrease to zero velocity at the wall consistent with the no-slip condition that is imposed.

To accurately determine the ignition time, τ_{ign} , the temperature maximum in the computational domain and glowplug surface temperature were monitored during the simulation. In the present study, ignition is defined as the time at which the maximum temperature in the domain reaches approximately 150 K above the glowplug surface temperature at that time. The inset in Figure 6 shows a close-up of the main heat release event. As early as $t = 4.29$ s, a small departure of the peak temperature from the prescribed temperature ramp is observed, which signals the start of significant heat release taking place away from the surface of the glowplug. Between $t = 4.465$ s and $t = 4.4675$ s the main heat release event occurs with the gas temperature peaking to ~ 2500 K. The time to ignition ($\tau_{ign} = 4.465$ s) corresponds to a glowplug surface temperature of ~ 1282 K. This numerical prediction is in agreement with the observed glowplug temperature at the time of ignition, $1275 \text{ K} \pm 45 \text{ K}$. The difference between observed and predicted values is 0.55% and taking into account uncertainties 2.88% and 4.23% of upper and lower bounds.

Ignition evolution

Two-dimensional fields are shown in Figure 7 of velocity, product mass fraction (P), and temperature together with velocity vectors and temperature contours at four instances during the simulation. The temperature contours are rescaled to cover the full range of temperature within the computational domain at each time. At $t = 4$ s, chemical activity is already taking place at the top of the glowplug where the temperature is highest, and convective losses are minimal. The temperature maximum in the domain ($T = 1180$ K) corresponds to that of the glowplug surface. At $t = 4.465$ s, 465 ms later, a region of strong chemical activity appears on the temperature field as closed contours above the top of the glowplug. The reaction rate is strong enough to overcome diffusive and convective losses and an internal maximum appears bringing the temperature to 1429 K, roughly ~ 150 K

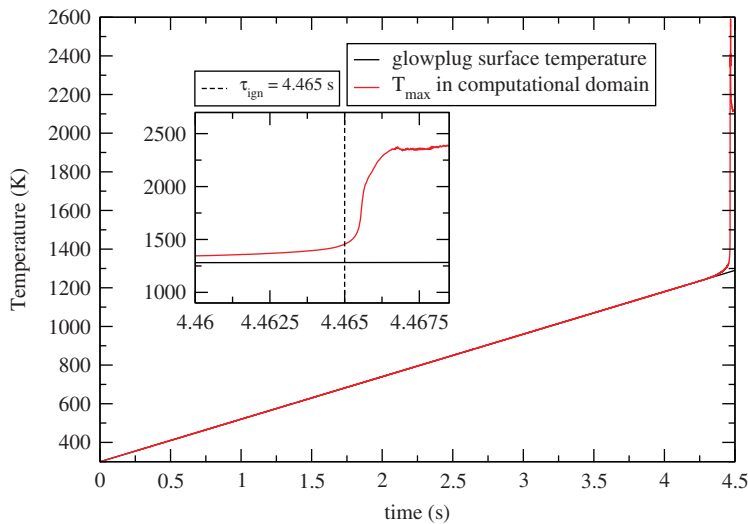


Figure 6. Glowplug temperature and temperature maximum in computational domain during the course of the simulation for a heating ramp of 220 K/s. Inset: close-up of ignition event.

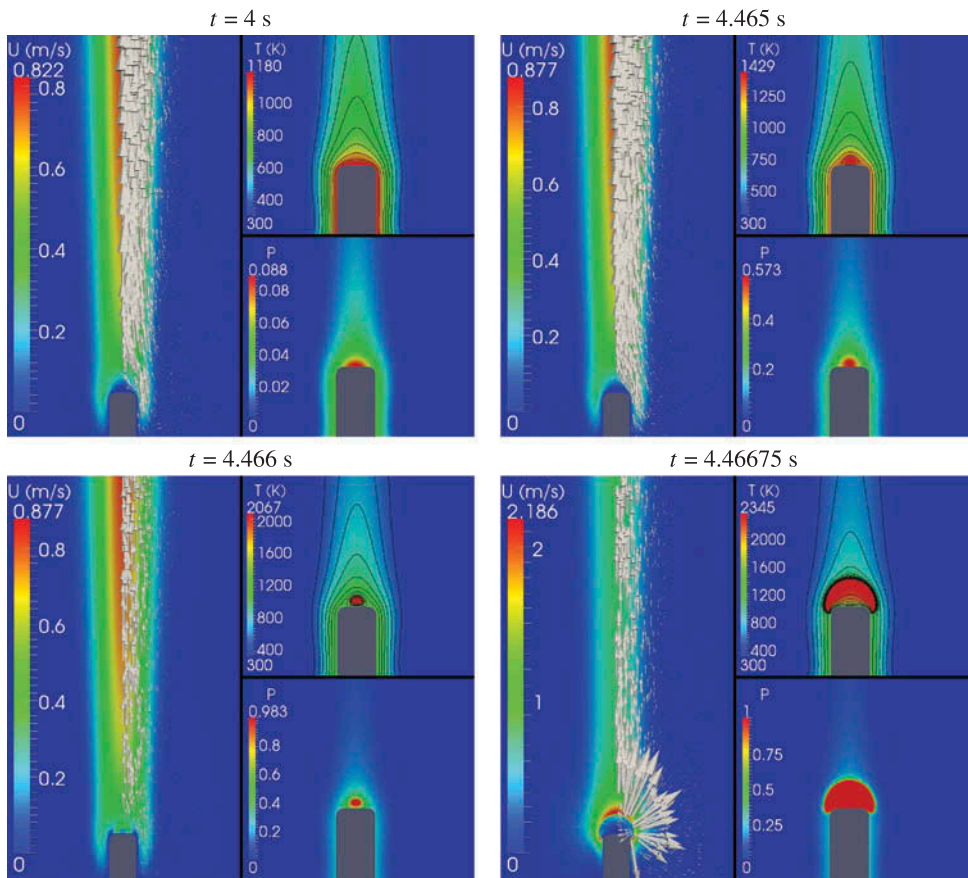


Figure 7. Velocity, product mass fraction, and temperature fields. Top left: at $t = 4$ s—near end of heating period. Top right: at $t = 4.465$ s—ignition event. Bottom left: at $t = 4.466$ s—1 ms after ignition/flame kernel formation. Bottom right: at $t = 4.46675$ s—early stages of flame propagation.

higher than the prescribed value at the glowplug surface. At $t = 4.466$ s, an ignition kernel forms. A nascent flame can be observed in the temperature contours, and the fuel is nearly completely consumed within the kernel, as the mass fraction of the product reaches 0.983. No change is seen in the magnitude of velocity because the maximum remains at the plume; however, initial displacement of the gas ahead of the ignition kernel is visible. The last frame, $t = 4.46675$ s, shows the early stages of flame propagation; the velocity vectors display how the surrounding gas is pushed radially outwards very rapidly. Acceleration of the gas from 0.877m/s to 2.186m/s in 0.75ms can be seen on the velocity fields. The maximum in velocity is now located immediately ahead of the flame, and the rapid expansion is evidenced by the size of the velocity vectors in the flow field. The shape of the flame is determined by the preferential propagation of the combustion front along the thermal plume where fresh combustible mixture is hottest. The temperature contours show clearly a nearly uniform high temperature region within the flame, except close to the glowplug surface where heat transfer occurs from combustion products towards the hot surface walls.

Discussion

Energy equation analysis

To gain additional insight into the processes important to ignition near the top of the glowplug, each of the terms in the energy conservation equation is plotted along its vertical centerline (see Figure 8). The plots are taken at the same times as in Figure 7 to allow for a direct comparison. The abscissas represent the vertical distance along the axis of symmetry measured from the top surface of the glowplug, whereas the ordinates show the corresponding energy density and temperature. The solid lines are the convective and diffusive heat losses, and the chemical source term given respectively by $h_{Convection} = -\nabla \cdot (\rho u h)$, $h_{Diffusion} = \nabla \cdot (\kappa / c_p \nabla h)$, and $h_{Source} = q_{chem} \dot{\Omega}_R$. The dashed line is the sum of the above terms, $h_{Unsteady}$, and the dashed-dotted line is the temperature. During the initial stages of heating (top left), the energy released by the chemistry is immediately balanced by diffusion close to the wall, and no contributions are due to convection as the gas is effectively at rest up to 1mm from the top of the glow plug. However, away from the wall, convection balances diffusion and the temperature is too low for significant chemical reaction to take place. The temperature maximum is at the wall. At $t = 4.465$ s, chemical reaction becomes significant and the balance is disrupted so that the net energy addition (sum term) is greater than zero up to 2mm away from the wall. The maximum in temperature moves away from the wall signaling that the rate at which heat is diffused to the glowplug surface is not large enough to counteract the rate at which heat is released by the chemical reaction. The dip in the convective term is due to a slight expansion of the gas in this region. At $t = 4.466$ s, the energy balance plot (lower left) shows that ignition occurs very close to the wall roughly at 0.6 mm; the structure of the ignition kernel and the birth of an expanding flame front is distinct. The rapid nature of the ignition event can be visualized in the 9-fold increase in the heat release rate occurring over 1ms. Finally, the bottom right plot in Figure 8 shows the typical structure of a laminar flame propagating away from the surface of the glowplug, with diffusion and convection in balance in the preheat zone, and the source term balanced by the combined effect of convection and diffusion in the energy release zone.

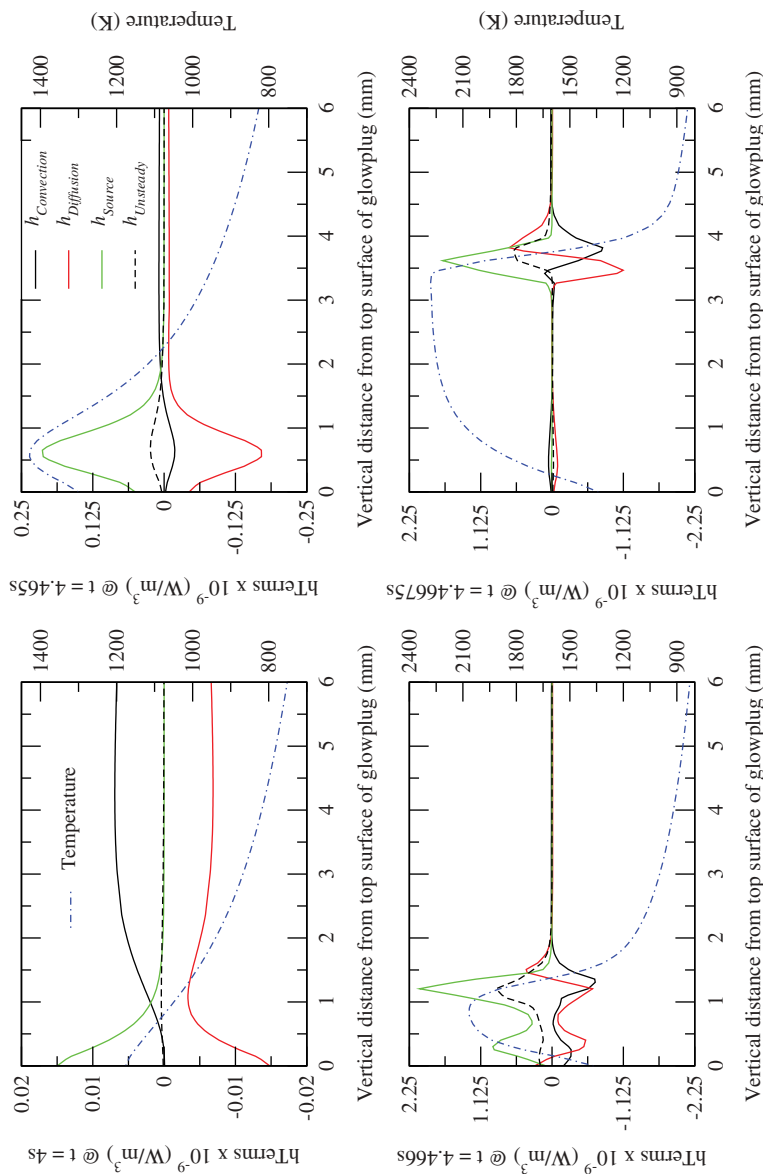


Figure 8. Contributions of each term in energy equation and temperature along vertical centerline of the glowplug. Top left: at $t = 4$ s—near end of heating period. Top right: at $t = 4.465$ s—ignition event. Bottom left: at $t = 4.466$ s—1 ms after ignition/flame kernel formation. Bottom right: at $t = 4.46675$ s—early stages of flame propagation.

Close-up to ignition location

Temperature probes above glowplug

A convenient way of visualizing the competition between energy losses and chemical heat release is by monitoring the evolution of temperature near the ignition location. Figure 9 shows temperature probes taken at different locations above the glowplug, namely, 0.1, 0.2, 0.3, 0.5, 0.6, 0.8, and 1 mm away. The entire process from early stages of heating to ignition is shown in the main plot. The insets show close-ups to the moment when the gas temperature surpasses the temperature ramp prescribed on the surface of the glowplug (left), and the main ignition event (right). At early times the process is mostly governed by diffusion with the parcel of gas closest to the surface of the glowplug (0.1 mm) having a temperature slightly less than the temperature ramp. With increasing distance from the surface, temperature is lower as it takes longer for thermal energy to diffuse to that location. Once significant chemical heat release occurs, the temperature of the gas rises above the prescribed temperature ramp sequentially as seen on the left inset. The temperature of the closest probe, 0.1 mm, exceeds the ramp temperature at $t = 4.3$ s, 0.2 mm at $t = 4.35$ s, 0.3 mm at $t = 4.375$ s, 0.5 mm at $t = 4.405$ s, 0.6 mm at $t = 4.425$ s, 0.8 mm at $t = 4.45$ s, and the furthest probe, 1 mm, crosses at $t = 4.475$ s. Although the probe at 0.1 mm (red solid line) exceeds the surface temperature first, the rate of temperature increase is not as high as for those probes located further away because of the close proximity to the glowplug, which results in higher diffusive losses to the heated surface.

The horizontal black dashed-dotted line on the right inset corresponds to the criteria for ignition given in the numerical results section. Close to the surface, any energy deposition in the gas is immediately counteracted by heat transfer back to the hot surface,

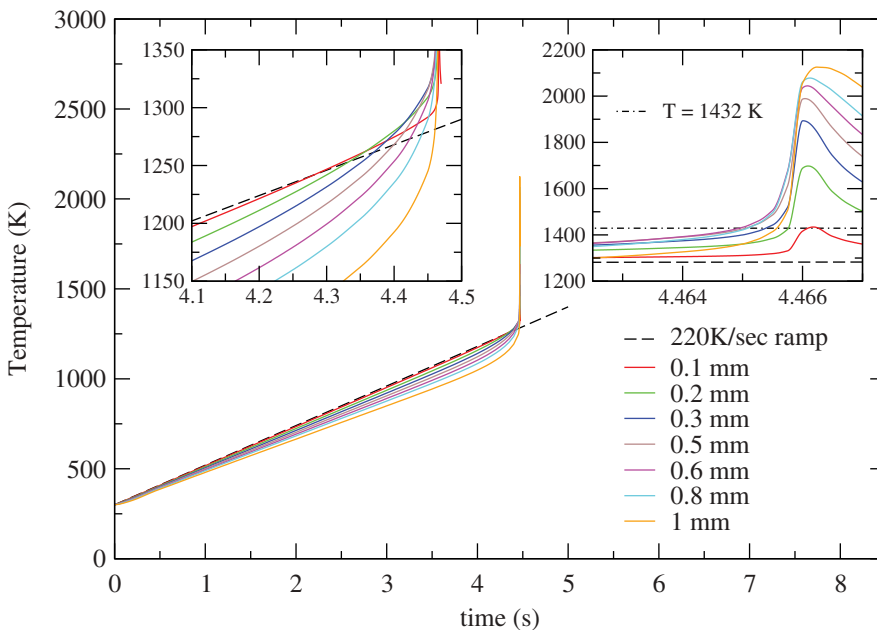


Figure 9. Temperature probes taken at different locations above the top surface of the glowplug. Insets: close-up to initial departure of gas temperature from ramp imposed on glowplug (left); close-up to ignition event (right).

inhibiting ignition. Further away, the gas temperature is not high enough for the chemical reaction rate to be sufficiently fast to trigger significant heat deposition. Additionally, convective losses become increasingly more important with increasing distance from the surface. Consistent with what was observed to be the center of the ignition kernel while analyzing the competition among the different terms in the energy equation (bottom left plot in Figure 8), the probe at 0.6 mm (magenta solid line) intersects the ignition criteria line of 1432 K first. Note that the parcel of gas closest to the glowplug (0.1 mm) never goes beyond the threshold level because diffusive losses is the dominant term at this location.

Comparison with experiments

The prediction of the hot surface ignition temperature was in reasonable agreement with experiments with a difference of less than 5%. Next, a quantitative comparison of the size and shape of the thermal plume, ignition kernel, and flame during the early stages of propagation is presented. In order to perform the comparison, the numerical density fields were postprocessed to compute the corresponding numerical optical phase difference $\Delta\phi$ as follows: the refractivity $n(r)$ (see Figure 3) was calculated using the Gladstone–Dale relation, Eq. (9), where $K = 2.274 \times 10^{-4} \text{ m}^3/\text{kg}$ at room temperature and atmospheric pressure (Merzkirch, 1987). The optical phase difference is then obtained by integrating over the optical path assuming axisymmetry (Eq. (10)):

$$\Delta\phi = 2 \int_x^\infty \frac{f(r)r}{(r^2 - x^2)^{1/2}} dr \quad \text{where} \quad f(r) = \frac{2\pi}{\lambda} [n(r) - n_o(r)] \quad (10)$$

Simulations were used to compare flow fields at times for which the flame tip advanced roughly the same distance along the vertical centerline as observed in the experiments. Comparing at actual physical times is not possible because the simplified kinetic mechanism reproduces ignition delay times and not flame speeds. The main purpose of this exercise is to confirm if the optical phase difference values obtained numerically agree well with those measured experimentally. The images at the top of Figures 10 and 11 show a side-by-side comparison of the optical phase difference $\Delta\phi$, and the graphs below show quantitative comparisons at fixed heights in the flow field: 8mm, 9.5mm, 11mm, 12.5mm, and 14 mm. The numerical and experimental results show the thermal plume, ignition kernel, and growth of the flame. Visually the optical phase difference fields are essentially indistinguishable, except for a slightly thicker plume. For instance, at $y = 22\text{mm}$, the green region in the plume goes beyond $x = -4\text{mm}$ in the experiments, whereas in the simulation, it fades before reaching $x = 4\text{mm}$. This asymmetry is also visible in the comparisons shown at the bottom of Figures 10 and 11. During the postprocessing, the undisturbed optical phase difference on one half of the experimental image is selected as the reference background noise, and subtracted from the full image. The offset between the experimental and numerical results at $x = 10\text{mm}$, where the flow is unaffected by the thermal plume, indicates a slightly different background noise level on the righthand side of the plot. Also, the small jumps in the experimental slices at 8 mm are artifacts of the postprocessing algorithm near solid boundaries. Overall, the flow field predicted numerically is in reasonable quantitative agreement with the experimental results.

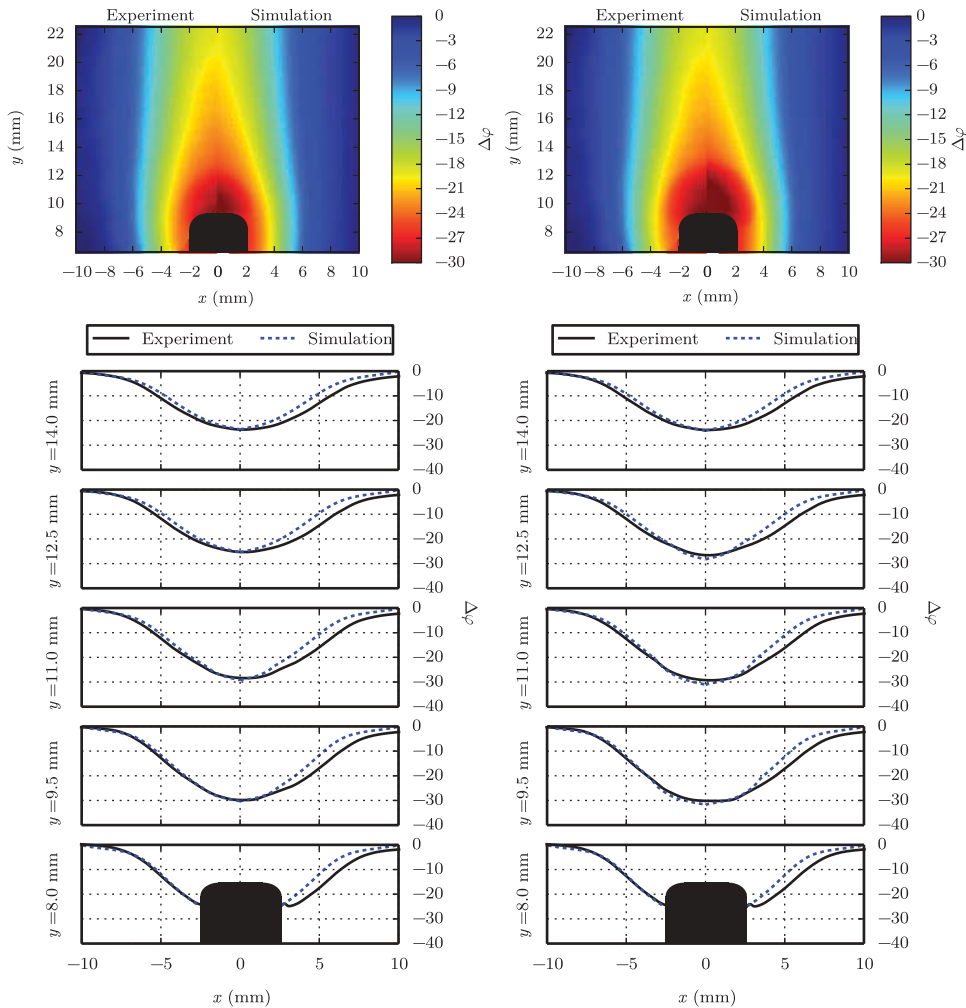


Figure 10. Quantitative comparison of experimental and numerical results during the ignition event at $p_o = 101$ kPa, $T_o = 300$ K, and $\Phi = 0.9$ *n*-hexane–air mixture. Top: optical phase difference ($\Delta\phi$) fields. Bottom: comparison of optical phase taken at different heights in the flow field: 8 mm, 9.5 mm, 11 mm, 12.5 mm, and 14 mm.

Conclusions

A 2D simulation of ignition over a rapidly heated surface was performed. Ignition was observed to occur at the top of the glowplug in both the experiments and simulations. The ignition evolution was explained in detail by means of velocity, product mass fraction, and temperature fields. Additional insight was achieved by analyzing the individual contributions of the terms in the energy conservation equation and by taking temperature probes at various locations above the top surface of the glowplug. Close to the wall, diffusion counteracts the heat release due to the chemistry, whereas far away, convection and diffusion maintain the balance. Significant chemical activity starts when the mixture temperature in the separated region above the glowplug rises over 1200 K; the parcels

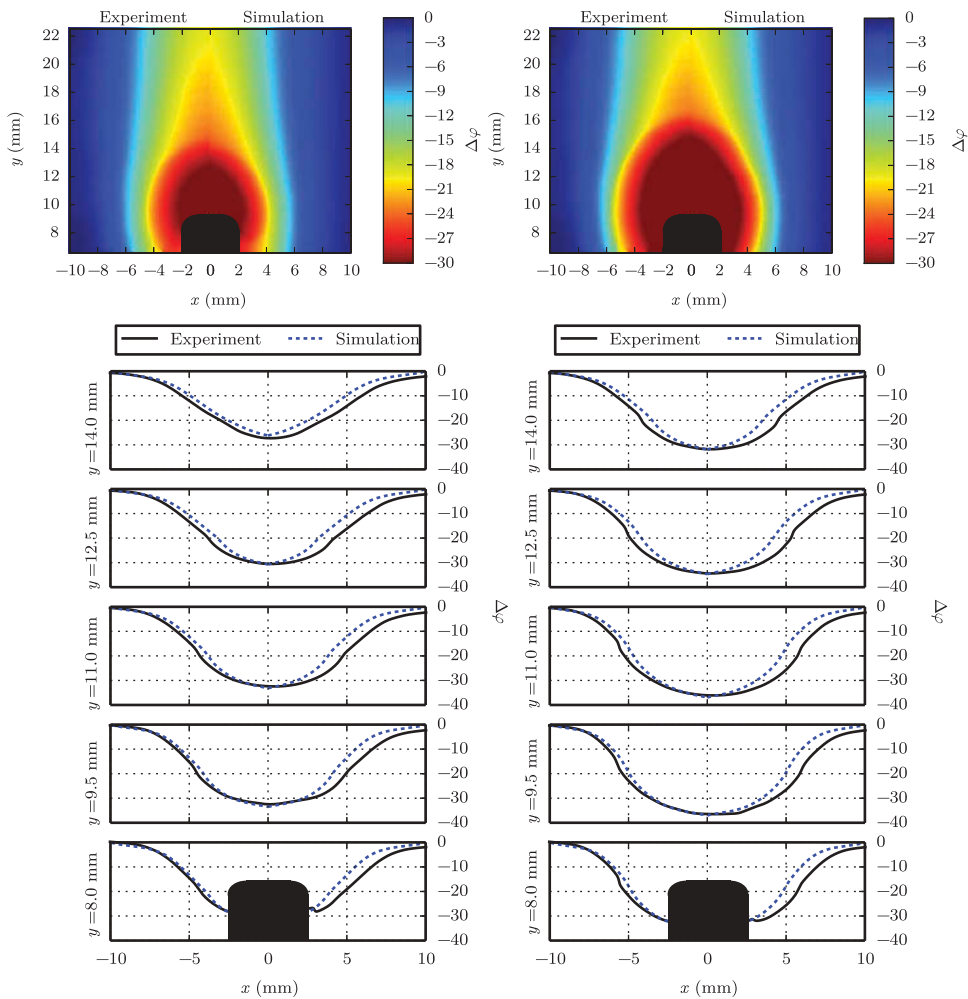


Figure 11. Quantitative comparison of experimental and numerical results during flame propagation: $p_o = 101$ kPa, $T_o = 300$ K, and $\Phi = 0.9$ *n*-hexane–air mixture. Top: optical phase difference ($\Delta\phi$) fields. Bottom: comparison of optical phase taken at different heights in the flow field: 8 mm, 9.5 mm, 11 mm, 12.5 mm, and 14 mm.

of gas in the stagnation volume have a long enough residence time for chemical rates to grow exponentially at high temperature. At 0.6 mm normal to the top of the glowplug surface, the heat release rate is greater than the rate at which heat is diffused back to the wall signaling the birth of an ignition kernel.

The overall quantitative agreement between the numerical predictions and experiments in terms of surface temperature at ignition, ignition location, and flow field features in the vicinity of the hot surface demonstrate the adequacy of the reduced chemical reaction model in simulating important aspects of the ignition process. Additionally, results show the importance of flow separation in creating zones/regions that are prone to ignition: convective transport of energy and species out of the separated region is minimized, and

the build up of species and energy can only be opposed by diffusion, facilitating the thermal run away characteristic of ignition.

The success of the simplified kinetic scheme in predicting the experimental ignition temperature emphasizes the importance and applicability of developing this type of models for use in multi-dimensional simulations of realistic geometries. Quantitative predictions of ignition thresholds for hot surfaces require a detailed simulation that includes correct initial and boundary conditions to capture important features, such as boundary layer separation and energy transport processes.

Finally, including additional physics, such as more complex chemical mechanisms (i.e., multi-step simplified chemistry) and surface reactions (i.e., adsorption of reactive species and/or catalytic effects), as well as a systematic variation of experimental parameters (i.e., heating rate, hot surface size, mixture equivalence ratio, etc.) and their effect on ignition thresholds were outside of the scope of this study and remain to be investigated in detail.

Acknowledgments

This work was carried out in the Explosion Dynamics Laboratory of the California Institute of Technology. Special thanks go to Dr. Lorenz Boeck and Andreas Kink for their help with the experimental setup and improving the quality of the diagnostics.

Funding

J. Melguizo-Gavilanes was supported by the Natural Sciences and Engineering Research Council of Canada (NSERC) Postdoctoral Fellowship Program. S. Coronel, R. Mével, and A. Nové-Josserand by the Boeing Company through a Strategic Research and Development Relationship Agreement CT-BA-GTA-1. This work used the Extreme Science and Engineering Discovery Environment (XSEDE), which is supported by the National Science Foundation grant number ACI-1053575.

References

- Adler, J. 1999. Ignition of a combustible stagnant gas layer by a circular hot spot. *Combust. Theor. Model.*, **3**(2), 359–369.
- Boettcher, P.A. 2012. Thermal ignition. PhD thesis. Caltech, Pasadena, CA.
- Boettcher, P.A., Menon, S.K., Ventura, B.L., Blanquart, G., and Shepherd, J.E. 2013. Cyclic flame propagation in premixed combustion. *J. Fluid Mech.*, **735**, 176–202.
- Coward, H.F., and Guest, P.G. 1927. Ignition of natural gas-air mixtures by heated metal bars 1. *J. Am. Chem. Soc.*, **49**(10), 2479–2486.
- Demirdzic, I., Lilek, Z., and Péric, M. 1993. A collocated finite volume method for predicting flows at all speeds. *Int. J. Numer. Methods Fluids*, **16**, 1029–1050.
- Gray, B.F. 1970. The dependence of spontaneous ignition temperature on surface to volume ratio in static systems for fuels showing negative temperature coefficient. *Combust. Flame.*, **14**(1), 113–115.
- Kemao, Q. 2004. Windowed Fourier transform for fringe pattern analysis. *Appl. Opt.*, **43**(13), 2695–2702.
- Kuchta, J.M., Bartkowiak, A., and Zabetakis, M.G. 1965. Hot surface ignition temperatures of hydrocarbon fuel vapor-air mixtures. *J. Chem. Eng. Data*, **10**(3), 282–288.
- Kumar, R.K. 1989. Ignition of hydrogen-oxygen-diluent mixtures adjacent to a hot, nonreactive surface. *Combust. Flame*, **75**(2), 197–215.
- Kuchta, J.M. 1985. Investigation of fire and explosion accidents in the chemical, mining, and fuel related industries. Bulletin 680. Bureau of Mines, Washington, DC.

- Laurendeau, N.M. 1982. Thermal ignition of methane-air mixtures by hot surfaces: A critical examination. *Combust. Flame*, **46**, 29–49.
- Law, C.K., and Law, H.K. 1979. Thermal-ignition analysis in boundary layer flows. *J. Fluid Mech.*, **92**(01), 97–108.
- Merzkirch, W. 1987. *Flow Visualization*, Academic Press, Orlando, FL.
- Mével, R., Chatelain, K., Boettcher, P. A., Dayma, G., and Shepherd, J.E. 2014. Low temperature oxidation of *n*-hexane in a flow reactor. *Fuel*, **126**, 282–293.
- Nestor, O.H., and Olsen, H.N. 1960. Numerical methods for reducing line and surface probe data. *SIAM Rev.*, **3**(2), 200–207.
- Ramirez, H., Hadj-Ali, K., Dievart, P., Dayma, G., Togbe, C., Moreac, G., and Dagaut, P. 2011. Oxidation of commercial and surrogate bio-diesel fuels (B30) in a jet-stirred reactor at elevated pressure: Experimental and modeling kinetic study. *Proc. Combust. Inst.*, **33**, 375–382.
- Rastogi, P. and Hack, E. 2015. *Phase Estimation in Optical Interferometry*, CRC Press, Boca Raton, FL.
- Semenov, N.N. 1940. Thermal theory of combustion and explosions. *Prog. Phys. Sci.* **23**(3), 251–292.
- Weller, H.G., Tabor, G., Jasak, H., and Fureby, C. 1998. A tensorial approach to continuum mechanics using object-oriented techniques. *Comput. Phys.*, **12**, 620–631.